Supporting Information

Amino-functionalized Pd-NH_2/WO_x(C) nanocatalysts with oxygen vacancy-rich for efficient formic acid dehydrogenation

Ziyang Hong, Dan Liu, Qikui Fan, Hao Lv, Zhimao Yang, Chuncai Kong*

Ministry of Education Key Laboratory for Non-equilibrium Synthesis and Modulation of Condensed Matter, Shaanxi Province Key Laboratory of Advanced Functional Materials and Mesoscopic Physics, School of Physics, Xi'an Jiaotong University, Xi'an, 710049, P. R. China.

*** Corresponding authors:**

E-mail: kongcc@xjtu.edu.cn (C. Kong)

Experimental section

1. Chemical and materials

Tungsten hexachloride (WCl_6), triethylene glycol ($C_6H_{14}O_4$), glucose ($C_6H_{12}O_6$), sodium chloropalladate (Na_2PdCl_4), (3-aminopropyl) triethoxysilane (APTS), and formic acid (FA, HCOOH) were purchased from Aladdin Reagents Ltd. Ethanol was purchased from FuYu Chemical Reagents. All reagents were used directly without further purification. The deionized water used in all experiments had a resistivity of 18.2 MΩ cm^{-1}.

2. Synthesis of WO_x(C) Nanowires

The WO_x(C) Nanowires support was synthesized according to the previous report with minor modifications.[1] First, 0.4 g of WCl_6 was dissolved in 40 mL of triethylene glycol, followed by the addition of 0.4 g of glucose under ultrasonic agitation. The corresponding glucose concentration was approximately 55.5 mM. The homogeneous precursor solution was transferred into a 100 mL PTFE-lined stainless-steel autoclave, corresponding to a filling ratio of 40%. The autoclave was maintained at 200 °C for 6 h in an electric oven and then naturally cooled to room temperature without forced cooling. The resulting WO_x(C) nanowires were collected by centrifugation, washed several times with anhydrous ethanol, and vacuum-dried at 70 °C for 12 h.

3. Synthesis of Pd-NH_2/WO_x(C) catalyst

First, 150 mg of WO_x(C) was added to 150 mL of deionized water and sonicated for 1 h, 0.1 mL of APTS was added to the solution, followed by sonication for 1 h and stirring for 1 h. Then, 6 mg of Na_2PdCl_4 was added to the mixed solution, stirred for 24 h, and then the resulting solution was stirred in a water bath at 80 °C for 30 min. Finally, the resulting Pd-NH_2/WO_x(C) catalyst was collected by centrifugation, washed repeatedly with anhydrous ethanol, and vacuum dried at 70 °C for 12 h. The preparation method for the comparison catalyst was similar to that of Pd-NH_2/WO_x(C). During the preparation of Pd-NH_2/WO_x, glucose was not added for carbon doping; during the preparation of Pd/WO_x(C), APTS was not added for amino modification.

4. Catalytic tests for FA dehydrogenation

The catalytic reaction of FA dehydrogenation was carried out in 10 mL sealed round bottom flask with strictly controlled temperature by a water bath. Typically, the 80 mg of catalysts were dispersed into 3 mL of ultrapure water with ultrasound for 30 min. The reaction was conducted at 298 K with 1.0 mL of FA solution (2.0 M) was injected into the above mixture solution with a syringe. The sealed round-bottom flask was connected to

an inverted measuring cylinder filled with water via a gas conduit to determine the volume of generated gas. The reaction thermodynamics of FA dehydrogenation was investigated by adjusting reaction temperature (298, 303, 313, 323, and 333 K), the kinetics were analyzed by changing the amount of catalyst (2.14, 2.75, 3.36 and 3.97 mM) and the concentrations of FA (0.25, 0.50, 0.75, and 1.00 mmol) added. The catalytic activity of the Pd-NH_2/WO_x(C) catalyst under higher concentration of formic acid (5 M, 10 M, 15 M, 20 M and 26 M (neat FA)) at room temperature are evaluated by adjusting the amount of water solvent added, with unchanged catalyst dosage and FA amount. Durability tests were performed at 298 K through repeating the reaction for another 4 times with the addition of equivalent of pure FA (2 mmol) into the reaction mixture after the last reaction was over. The TOF values were calculated based on the total molar amount of Pd determined by Inductively coupled plasma atomic emission spectroscopy (ICP-MS). The initial turnover frequency (TOF) was calculated using the following equations:

$$TOF_{initial} = \frac{P_{atm}V_{gas}}{2RTn_{metal}t}$$

where P_{atm} refers to the atmospheric pressure (101325 Pa), V_{gas} is the volume of final released gas (CO_2+H_2), R denotes the universal gas constant (8.3145 m^3 Pa mol^{-1} K^{-1}), T represents the room temperature (298 K), n_{metal} is the total molar number of Pd in catalyst, and t represents the reaction time when the conversion of FA is 20%.

5. Characterization

Transmission electron microscopy (TEM), high-angle annular dark-field scanning transmission electron microscopy (HAADF-STEM) and element energy dispersive spectroscopy (EDS) mapping images were taken on JEOL JEM-2100 and Talos-F200X, and JEM-ARM300F2 equipment. Scanning electron microscopy (SEM) was performed using a JSM-7000F scanning electron microscope. The X-ray diffraction (XRD) measurements were carried out on a D/Max-3c (Rigaku) X-ray diffractometer using Cu Kα radiation source (λ = 1.5406 Å). Nitrogen (N_2) sorption isotherms of catalysts were recorded on a micromeritics TriStar II 3020. Raman measurements were acquired on a HR800 Raman spectrometer using a 633 nm laser excitation. X-ray photoelectron spectra (XPS) spectra were carried out on a Thermo Fisher Scientific ESCALAB Xi+ spectrometer with an Al Kα radiator. Fourier transform infrared (FTIR) spectra of the samples were measured

on Bruker INVENIO X Spectrometer at room temperature. Inductively coupled plasma atomic emission spectroscopy (ICP-MS) were conducted on a NexION 350D equipment. The generated gas from FA dehydrogenation was determined by a North Point NP-GC-901A gas chromatograph (GC). Electron paramagnetic resonance (EPR) plots were recorded on a A300-10/12 (Bruker, Germany). All samples were measured using the same sample mass and identical instrumental parameters, and the EPR signal intensities were normalized by sample mass before comparison. For the temperature-programmed H_2 reduction (H_2-TPR), the samples were pretreated at 150 °C for 30 min under He flow and cooled down to 50 °C, and then the flowing gas was switched to 10% H_2/Ar for 30 min. Subsequently, the samples were purged with He flow for 30 min, and then heated to 800 °C with a heating rate of 15 °C/min under He flow.

6. DFT calculation

DFT calculations were performed using the VASP (Vienna Ab-initio Simulation Package) software.[2,3] The exchange correlation energy was approximated using the Perdew-Burke-Ernzerhof (PBE) functional under the Generalized Gradient Approximation (GGA).[4] The height of the vacuum layer along the z-axis was set to 20 Å. The Projector Augmented Wave (PAW) potential was selected to describe the atomic system,[5] and a plane wave basis set with a kinetic energy cutoff of 500 eV was used to account for valence electrons. To account for long-range dispersion interactions in the system, van der Waals corrections were applied using the Grimme DFT-D3 method (IVDW = 11). The WO_x support was constructed using a five-layer slab model with a slab thickness of approximately 7.3 Å. To reduce interactions between periodic images, a 3 × 3 × 1 surface supercell model was constructed. A vacuum layer of 20 Å was applied along the direction perpendicular to the surface to eliminate interlayer interactions caused by periodic boundary conditions. Brillouin-zone integration was performed using a 3 × 3 × 1 Monkhorst-Pack k-point mesh. During all structural optimizations, only the atomic positions were allowed to relax. The electronic self-consistent convergence criterion was set to 1×10^{-6} eV, and ionic relaxation was considered converged when the maximum Hellmann-Feynman force on each atom was less than 0.02 eV $Å^{-1}$.

The most stable configuration was determined by comparing the total energies of different adsorption sites, including top sites, bridge sites, and vacancy-adjacent sites. For the oxygen-vacancy model, oxygen-defect sites were constructed by removing oxygen atoms from the surface active region, followed by full geometry

optimization to obtain thermodynamically stable oxygen-vacancy configurations. During adsorption-configuration optimization, HCOOH molecules and the key reaction intermediate HCOO* were placed at multiple possible adsorption sites with different orientations for a global search. The most stable adsorption structures with the lowest total energies were finally selected for subsequent analysis. The adsorption energy was calculated according to the following equation:

$$E_{ads} = E_{(surface + adsorbate)} - E_{surface} - E_{adsorbate}$$

where $E_{(surface + adsorbate)}$, $E_{surface}$, and $E_{adsorbate}$ represent the total energies of the adsorption system, the clean surface, and the isolated adsorbate, respectively. A more negative value indicates stronger adsorption.

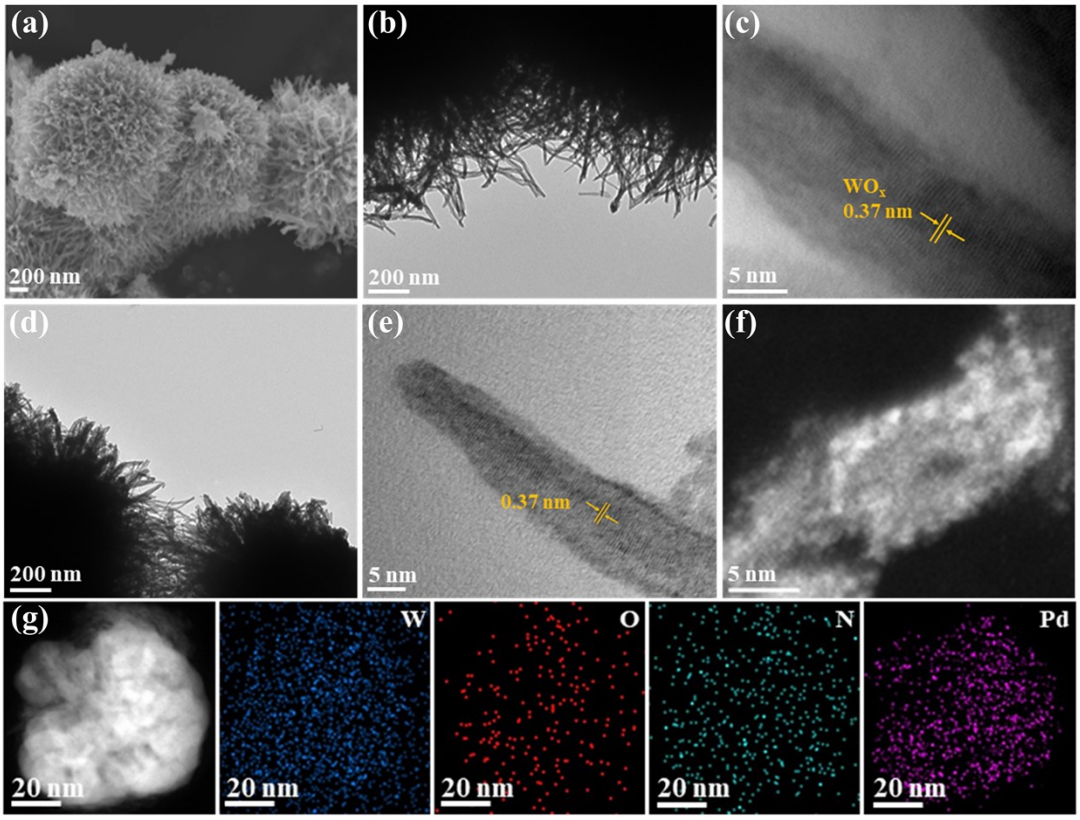

Figure S1. (a) SEM images, (b) TEM images, (c) HR-TEM images of WO_x. (d) TEM images, (e) HR-TEM images, (f) HAADF-TEM images of Pd-NH_2/WO_x. (g) Elemental mapping images for W, O, N and Pd in Pd-NH_2/WO_x.

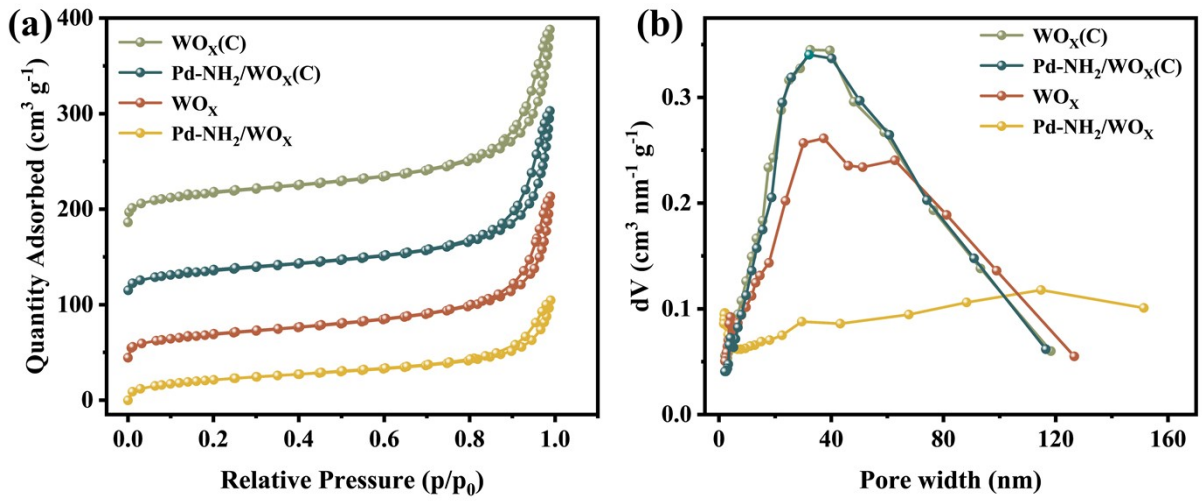

Figure S2. (a) Nitrogen adsorption-desorption isotherms, (b) corresponding pore distribution curves.

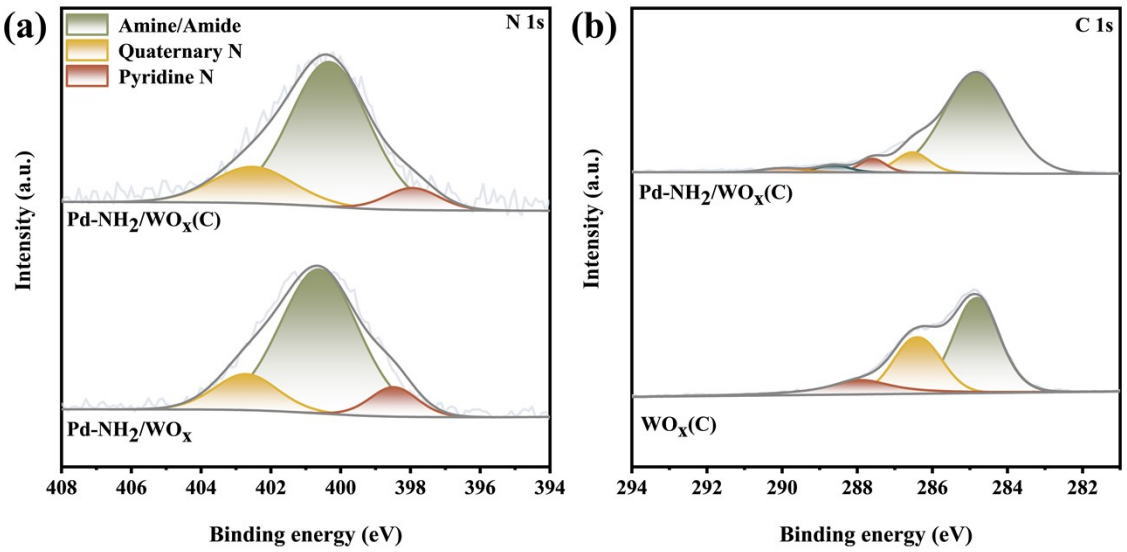

Figure S3. (a) N 1s XPS spectra of Pd-NH_2/WO_x and Pd-NH_2/WO_x(C). (b) C 1s XPS spectra of WO_x(C) and Pd-NH_2/WO_x(C).

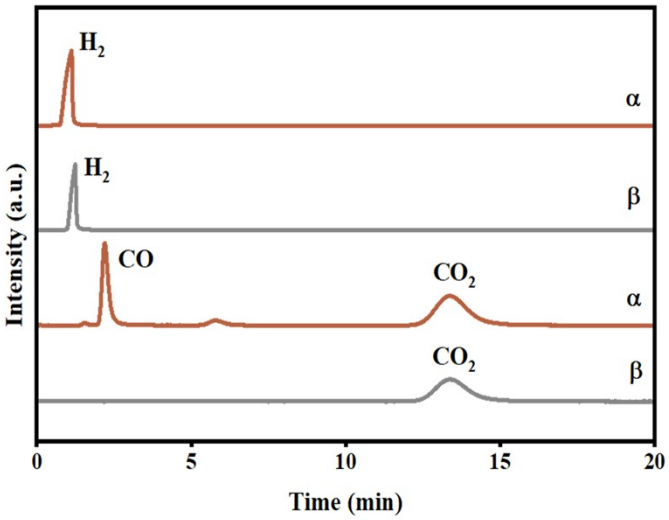

Figure S4. Gas chromatography analysis results for commercial mixed standard gas (α), and gas generated from FA (β).

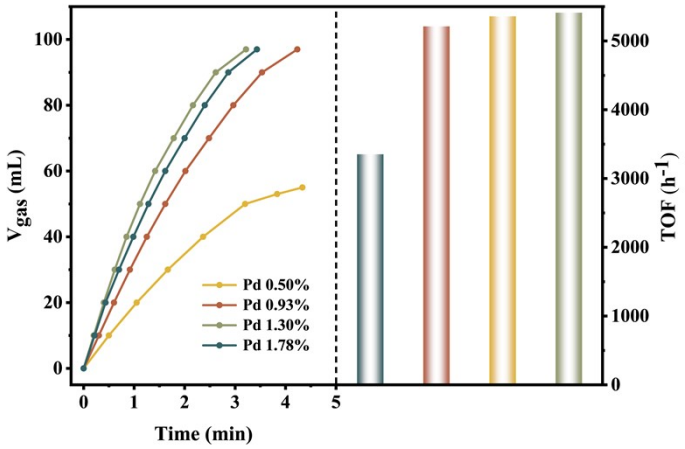

Figure S5. Gas generation plots and corresponding TOF over Pd-NH_2/WO_x(C) with different Pd contents.

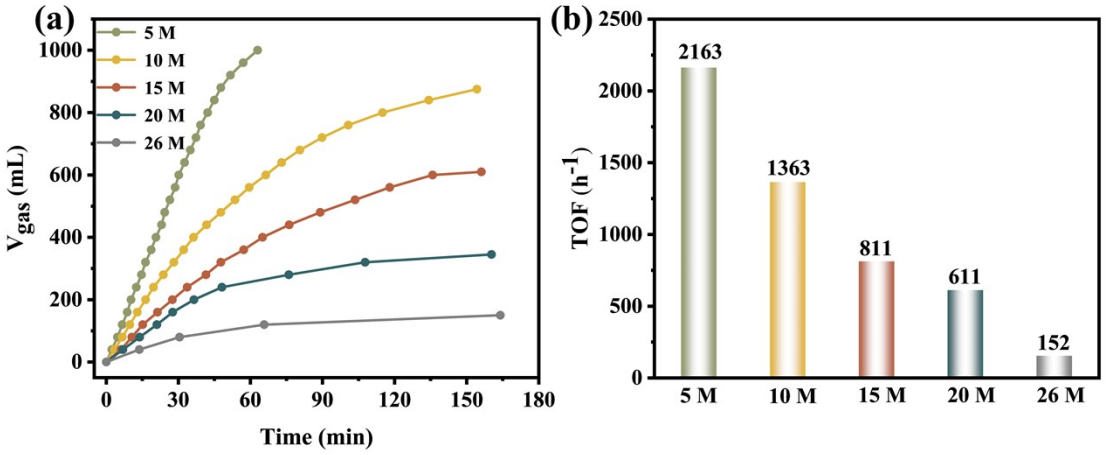

Figure S6. (a) Gas generation plots and (b) corresponding TOF over Pd-NH_2/WO_x(C) at different FA concentration.

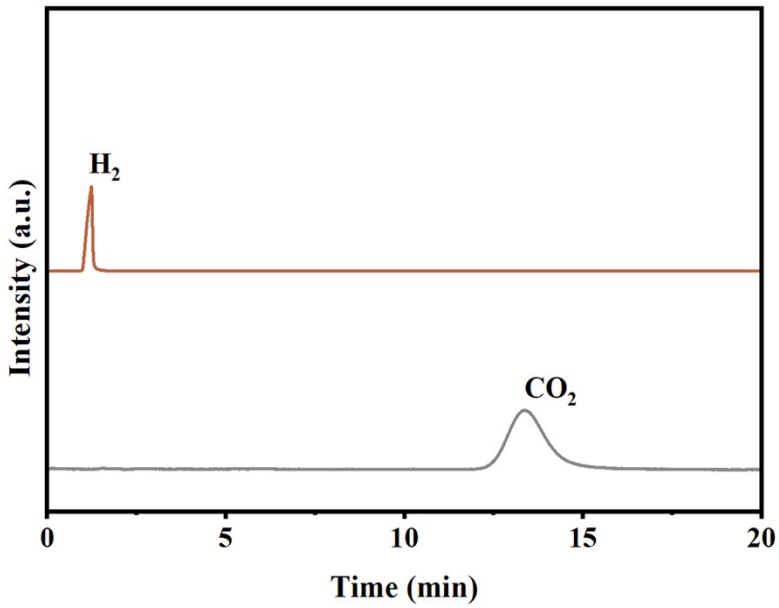

Figure S7. Gas chromatography analysis results for gas generated from FA dehydrogenation in the fifth reaction.

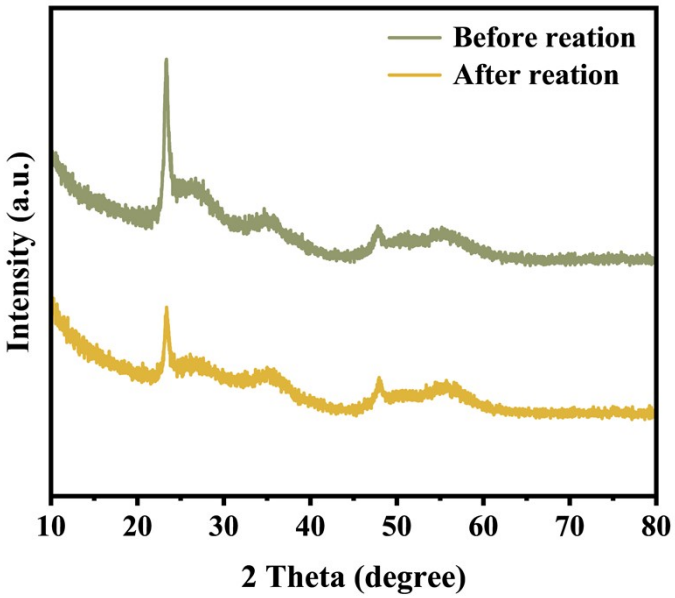

Figure S8. The XRD results of Pd-NH_2/WO_x(C) catalyst after five cycles of testing.

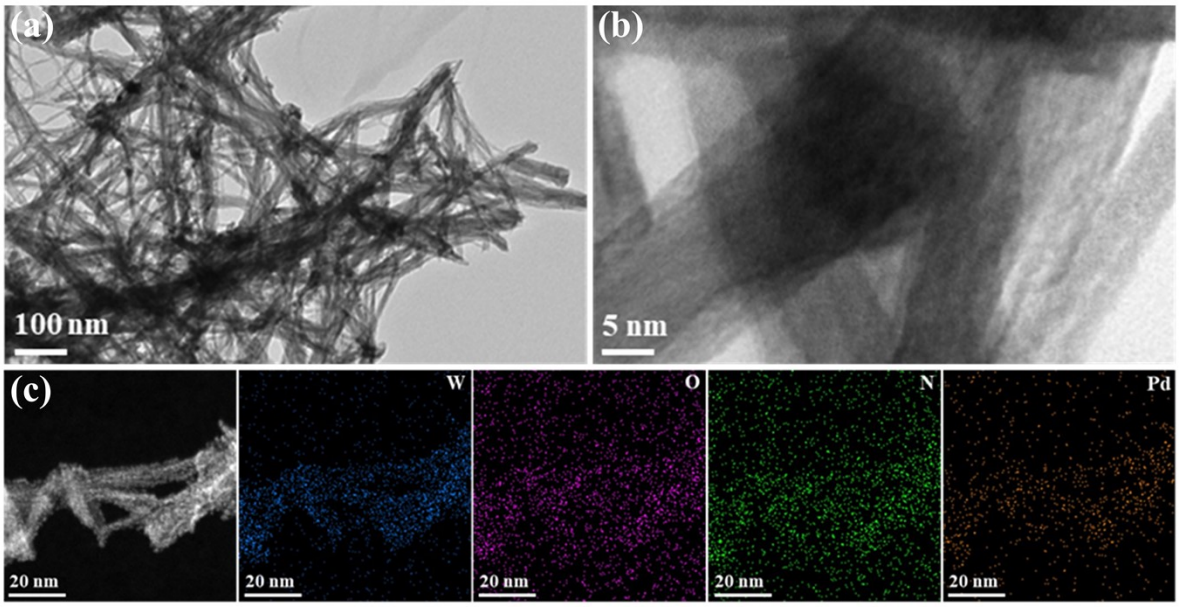

Figure S9. (a) TEM image, (b) HR- TEM image, and (c) EDS mapping images of Pd-NH_2/WO_x(C) catalyst after five cycles of testing.

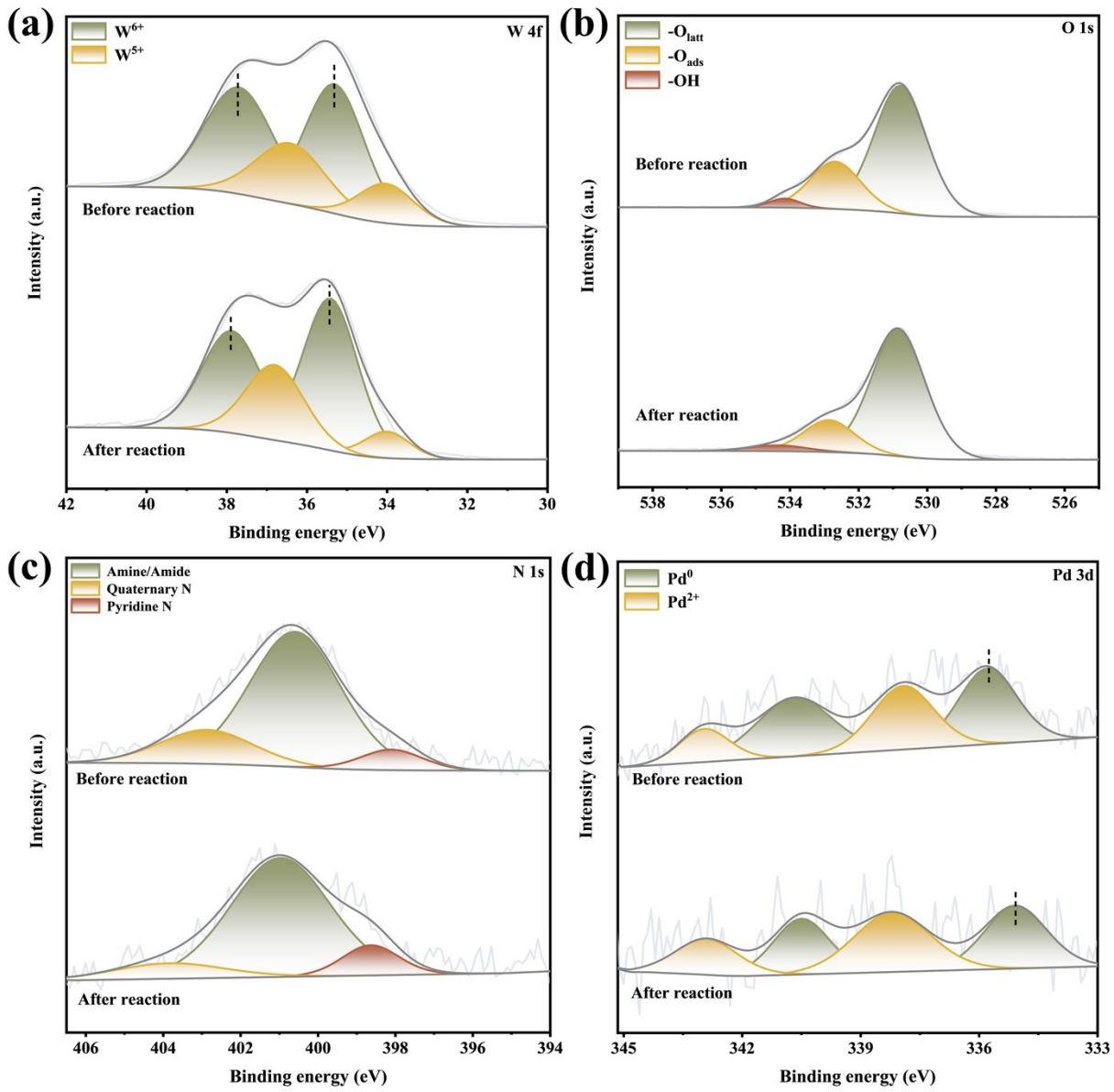

Figure S10. (a) W 4f, (b) O 1s, (c) N 1s, and (d) Pd 3d XPS spectra of Pd-NH_2/WO_x(C) catalyst after five cycles of testing.

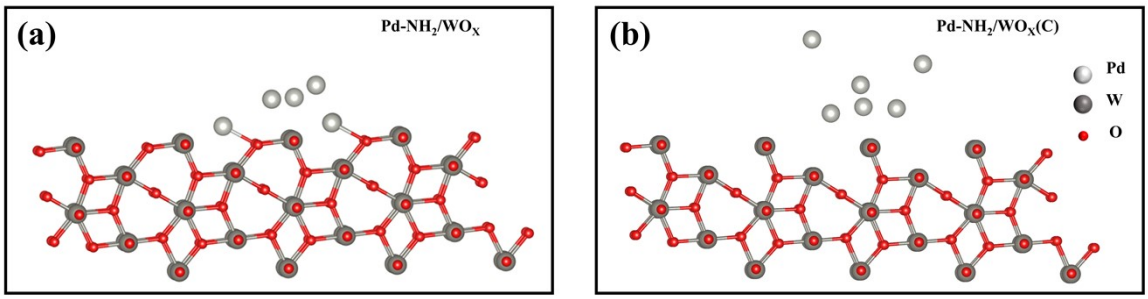

Figure S11. Slab model of (a) Pd-NH_2/WO_x, (b) Pd-NH_2/WO_x(C) for DFT calculation.

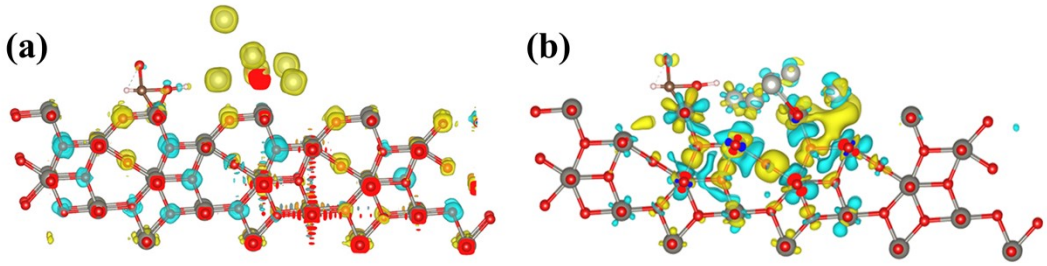

Figure S12. (a) Charge density difference of HCOOH* absorbed Pd-NH_2/WO_x (yellow and cyan represent electron accumulation and electron depletion, respectively). (b) Charge density difference of HCOOH* absorbed Pd-NH_2/WO_x(C).

Table S1. Comparison of key parameters of Pd-NH_2/WO_x for FA dehydrogenation with other reported catalysts.

Catalysts	Temp. (K)	Additive	E_a (kJ/mol)	TOF (h^{-1})	Ref.
Pd-NH_2/WO_x(C)	298	None	26.6	5412	This work
Pd@NH_2-NC	298	None	28.5	4892	[6]
Ag_2Pd_8/TiO_2-M-450	333	HCOONa	35.52	4789	[7]
$Au_{0.5}Pd_{0.5}$/NH_2-N-rGO	298	None	-	4445.6	[8]
PdNi-WO_x/KIT-6-NH_2	323	None	34.6	4417	[9]
Pd/NH_2-TPC	298	None	24.6	4312	[10]
$Au_{0.4}Pd_{0.6}$/PEI-PDA@CNCs	323	HCOONa	53.55	4258	[11]
$Pd_{60}Au_{40}$/HPC-NH_2	298	None	30.6	3763	[12]
Pd/MSC-30	323	HCOONa	38.6	2623	[13]
Pd-MnO_x/SiO_2-NH_2	333	None	61.9	2150	[14]
$Cr_{0.4}Pd_{0.6}$/MIL-101-NH_2	323	None	43.5	2009	[15]
Pd/NHPC-NH_2	298	None	46.3	1265	[16]
$Ni_{0.4}Pd_{0.6}$/NH_2-N-rGO	298	None	-	954.3	[17]

Table S2. Actual Pd loadings of different Pd-containing catalysts determined by ICP-MS.

Sample	Actual Pd loadings
Pd-NH_2/WO_x(C)	1.30 wt%
Pd-NH_2/WO_x	1.33 wt%
Pd/WO_x(C)	1.24 wt%

References

1 S. Zhang, H. Yang, H. Huang, H. Gao, X. Wang, R. Cao, J. Li, X. Xu and X. Wang, *J. Mater. Chem. A*, 2017, **5**, 15913-15922.

2 G. Kresse and J. Furthmüller, *Phys. Rev. B*, 1996, **54**, 11169-11186.

3 G. Kresse and J. Furthmüller, *Comput. Mater. Sci.*, 1996, **6**, 15-50.

4 J. P. Perdew, K. Burke and M. Ernzerhof, *Phys. Rev. Lett.*, 1996, **77**, 3865-3868.

5 P. E. Blöchl, *Phys. Rev. B*, 1994, **50**, 17953-17979.

6 D. Liu, C. Zhou, G. Wang, Y. Li, Z. Yang, C. Kong and B. Liu, *Chem. Synth.*, 2023, **3**, 24.

7 X. Sun, F. Li, Z. Wang, H. An, W. Xue and Y. Wang, *ChemCatChem*, 2022, **14**, e202101528.

8 S.-J. Li, Y.-T. Zhou, X. Kang, D.-X. Liu, L. Gu, Q.-H. Zhang, J.-M. Yan and Q. Jiang, *Adv. Mater.*, 2019, **31**, 1806781.

9 W.-F. Peng, X. Sun, Y. Ding, P. Liu, Q. Yao and Z.-H. Lu, *ACS Sustain. Chem. Eng.*, 2023, **11**, 1898-1908.

10 X. Shao, X. Miao, F. Tian, M. Bai, X. Guo, W. Wang, Z. Zhao, X. Ji, M. Li and F. Deng, *J. Energy Chem.*, 2023, **76**, 249-258.

11 J. Shen, Y. Liang, C. Wang and Y. Zhu, *Chem. Eng. J.*, 2023, **473**, 144640.

12 Z. Wang, S. Liang, X. Meng, S. Mao, X. Lian and Y. Wang, *Appl. Catal. B Environ*, 2021, **291**, 120140.

13 Q.-L. Zhu, N. Tsumori and Q. Xu, *Chem. Sci.*, 2014, **5**, 195-199.

14 A. Bulut, M. Yurderi, Y. Karatas, M. Zahmakiran, H. Kivrak, M. Gulcan and M. Kaya, *Appl. Catal. B Environ*, 2015, **164**, 324-333.

15 D. Gao, Z. Wang, C. Wang, L. Wang, Y. Chi, M. Wang, J. Zhang, C. Wu, Y. Gu, H. Wang and Z. Zhao, *Chem. Eng. J.*, 2019, **361**, 953-959.

16 Z. Wang, C. Wang, S. Mao, Y. Gong, Y. Chen and Y. Wang, *J. Mater. Chem. A*, 2019, **7**, 25791-25795.

17 J.-M. Yan, S.-J. Li, S.-S. Yi, B.-R. Wulan, W.-T. Zheng and Q. Jiang, *Adv. Mater.*, 2018, **30**, 1703038.